

Dynamic Josephson Junction Metasurfaces for Multiplexed Control of Superconducting Qubits

Mustafa Bakr^{1, *}

¹*Department of Physics, Clarendon Laboratory, University of Oxford, Oxford OX1 3PU, United Kingdom*

Scaling superconducting quantum processors to large qubit counts faces challenges in control signal delivery, thermal management, and hardware complexity, particularly in achieving microwave signal multiplexing and long-distance quantum information routing at millikelvin (mK) temperatures. We propose a space-time modulated Josephson Junction (JJ) metasurface architecture to generate and multiplex microwave control signals directly at mK temperatures. Theoretical and numerical results demonstrate the generation of multiple frequency tones with controlled parameters, enabling efficient and scalable qubit control while minimizing thermal loads and wiring overhead. We derive the nonlinear wave equation governing this system, simulate beam steering and frequency conversion, and discuss the feasibility of experimental implementation.

I. INTRODUCTION

Solid-state quantum processors such as superconducting qubits [1] and semiconductor quantum dots [2] operate at millikelvin temperatures to initialise the system in their ground state and prevent thermal excitation during operation. Initialisation, control, and measurement are routinely executed using classical control electronics generating microwave pulses [21, 22]. Scaling these approaches from the few-qubit level to large-scale quantum processors introduces challenges beyond just space limitations [3, 5]. Significant passive and active heat loads due to the dissipation of control signals in cables and attenuators are major concerns. These issues become more pronounced as scaling requires an increasing number of microwave and DC cables to be integrated into the dilution refrigerator (DL).

These requirements compete against the limited cooling power of the DL, typically around 20 μ W [6]. Thus, with current technologies, one could imagine systems with a few thousand qubits at best, far from the threshold necessary for a fault-tolerant universal quantum computer [9]. These critical challenges have motivated new approaches, ranging from building DRs with larger cooling capacities to introducing photonic links employing optical fibers to guide modulated laser light from room temperature to a cryogenic photodetector for delivering microwave signals at millikelvin temperatures [7, 26], and developing cryogenic CMOS electronics [8]. While advancements in photonic links and cryogenic CMOS electronics have been significant, issues such as active heating loads, thermal noise, and frequency conversion remain longstanding challenges [10, 23–25, 27]. Another promising approach for cryogenic control is Single Flux Quantum (SFQ) logic, which operates at ultra-fast speeds with low power consumption, making it highly suitable for qubit control. However, SFQ faces challenges, including precision timing control and signal crosstalk, especially in multi-qubit systems [11, 12]. Researchers are

actively developing solutions, such as advanced circuit designs and shielding techniques, to address these issues, but achieving scalable, high-fidelity control remains an open question [15]. Indeed, a low-power cryogenic architecture capable of generating classical signals suitable for high-fidelity qubit operation combined with multiplexing and non-reciprocal functionalities could be instrumental in building a large-scale quantum computer.

In this work, we propose a dynamic metasurface architecture utilising Josephson Junctions (JJs) to generate and multiplex microwave control signals directly at millikelvin temperatures. Our approach consists of a two-dimensional (2D) metasurface composed of an $N \times N$ square lattice of capacitively shunted JJs, as illustrated in Fig. 1 (d & e). This cQED metasurface is designed to be compatible with various quantum circuit architectures, potentially allowing coupling to qubits in free space or on-chip and replacing the heavily attenuated coaxial cables with a single RF coaxial line and multiple DC lines, as shown in Fig. 1 (a & b), significantly reducing both passive and active heat loads. By modulating the Josephson inductance both spatially and temporally [4], we enable dynamic control over the frequency, amplitude, phase, and spatial distribution of generated signals. We derive a nonlinear wave equation governing the system's dynamics, revealing unique phenomena such as beam steering and frequency conversion. Through numerical simulations, we demonstrate the generation of multiple frequency tones with controlled parameters, validating the potential of our approach for efficient, scalable qubit control. Our work lays the foundation for a new paradigm in cryogenic signal generation and routing, potentially overcoming key bottlenecks in quantum computer scalability.

II. NONLINEAR WAVE EQUATION WITH TIME-SPACE MODULATION

In this section, we derive the nonlinear wave equation governing the dynamics of a capacitively shunted Josephson Junction (JJ) transmission line, as depicted

* mustafa.bakr@physics.ac.uk

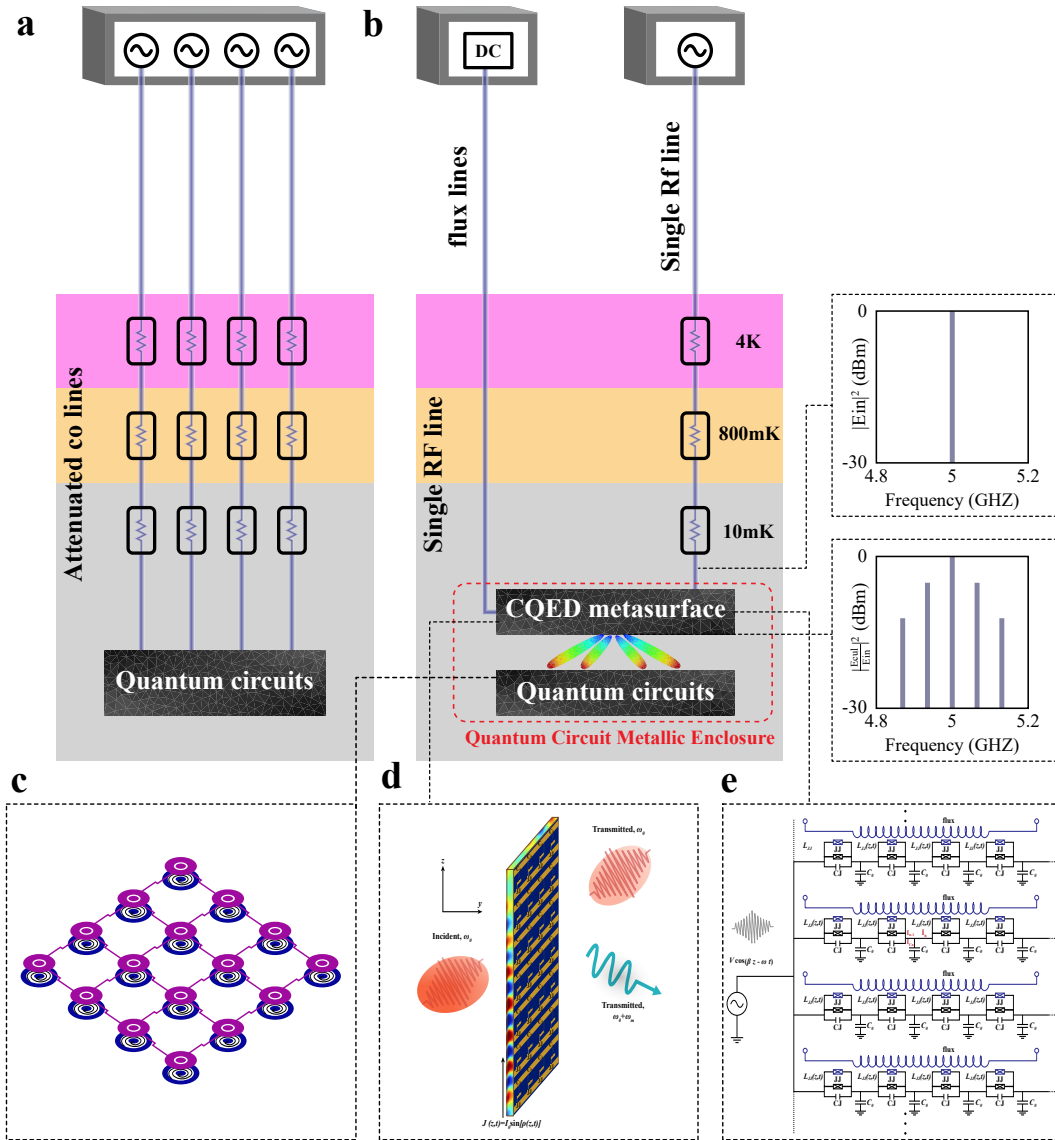


FIG. 1. a) Schematic of a conventional wiring approach using coaxial cables, room-temperature microwave generators (AWG), and heavily attenuated coaxial lines connected to the quantum circuit at millikelvin temperatures. The system experiences both passive heat from the thermal conductivity of the coaxial lines and active heat from power dissipation in the attenuators. (b) The cQED metasurface approach, which minimizes hardware overhead by using a single microwave link, multiple DC lines, and a single room-temperature microwave generator, with signals routed directly to the cQED metasurface via an attenuated coaxial line to millikelvin temperatures. The metasurface generates multiple microwave signals at the quantum circuit level with controllable frequency, amplitude, and spatial angle, significantly reducing both passive and active heat loads. (c) Inset: A false-color illustration of a 16-qubit superconducting quantum processor with nearest-neighbour coupling. (d) Inset: The cQED metasurface architecture, consisting of an $N \times N$ square lattice of capacitively shunted Josephson junctions (JJs), coupled to the quantum processor in free space. (e) The equivalent circuit. The metasurface can be designed using JJs or SQUIDs for tunability, with flux loops as shown in the blue circuits added to the diagram.

in Fig. 1(d & e). This derivation lays the groundwork for understanding how modulation of the JJ inductance influences beam control, frequency conversion, and qubit multiplexing. We consider a discrete transmission line composed of identical unit cells of length a . Each unit

cell consists of an inductor $L_J(z, t)$ and a capacitor C , where $L_J(z, t)$ varies both in space and time due to an applied DC flux $\Phi_{\text{ext}}(z)$ and an AC modulation signal (RF pump) that modulates the phase difference across the Josephson Junction. The critical current $I_c(t)$ of the

JJ is modulated by an external RF signal, leading to:

$$I_c(t) = I_{c0} \cos(\theta(z) + \Delta\varphi \cos(\omega_{\text{RF}}t)), \quad (1)$$

where I_{c0} is the maximum critical current, $\theta(z) = \frac{\pi\Phi_{\text{ext}}(z)}{\Phi_0}$ is the static phase shift across the junction due to the applied DC flux $\Phi_{\text{ext}}(z)$, $\Delta\varphi$ represents the modulation depth in phase due to the RF pump, ω_{RF} is the frequency of the RF modulation, and $\Phi_0 = \frac{h}{2e}$ is the magnetic flux quantum. The Josephson inductance $L_J(z, t)$ is related to the critical current by:

$$L_J(z, t) = \frac{\Phi_0}{2\pi I_c(t)} = \frac{\Phi_0}{2\pi I_{c0} \cos(\theta(z) + \Delta\varphi \cos(\omega_{\text{RF}}t))}. \quad (2)$$

To include higher-order harmonics introduced by the modulation, we use the trigonometric identity for the cosine of a sum:

$$\cos(\theta(z) + \Delta\varphi \cos(\omega_{\text{RF}}t)) = \cos\theta(z) \cos(\Delta\varphi \cos(\omega_{\text{RF}}t)) - \sin\theta(z) \sin(\Delta\varphi \cos(\omega_{\text{RF}}t)). \quad (3)$$

Assuming that $\theta(z)$ is chosen such that $\sin\theta(z) = 0$ (i.e., $\theta(z) = n\pi$ with $n \in \mathbb{Z}$), the sine term vanishes, and the expression simplifies to:

$$\cos(\theta(z) + \Delta\varphi \cos(\omega_{\text{RF}}t)) = \cos\theta(z) \cos(\Delta\varphi \cos(\omega_{\text{RF}}t)). \quad (4)$$

Therefore, the Josephson inductance becomes:

$$L_J(z, t) = \frac{\Phi_0}{2\pi I_{c0} \cos\theta(z) \cos(\Delta\varphi \cos(\omega_{\text{RF}}t))}. \quad (5)$$

We use the Jacobi-Anger expansion to express $\cos(\Delta\varphi \cos(\omega_{\text{RF}}t))$ as:

$$\cos(\Delta\varphi \cos(\omega_{\text{RF}}t)) = J_0(\Delta\varphi) + 2 \sum_{n=1}^{\infty} J_{2n}(\Delta\varphi) \cos(2n\omega_{\text{RF}}t). \quad (6)$$

Alternatively, since $\Delta\varphi$ is small, we can expand the denominator using a Taylor series for $\cos x$:

$$\cos x = 1 - \frac{x^2}{2} + \frac{x^4}{24} - \dots \quad (7)$$

Substituting $x = \Delta\varphi \cos(\omega_{\text{RF}}t)$:

$$\begin{aligned} \cos(\Delta\varphi \cos(\omega_{\text{RF}}t)) &= 1 - \frac{(\Delta\varphi \cos(\omega_{\text{RF}}t))^2}{2} \\ &\quad + \frac{(\Delta\varphi \cos(\omega_{\text{RF}}t))^4}{24} - \dots \end{aligned} \quad (8)$$

Using trigonometric identities for $\cos^2(\omega_{\text{RF}}t)$ and $\cos^4(\omega_{\text{RF}}t)$, we can further expand and obtain:

$$\begin{aligned} \cos(\Delta\varphi \cos(\omega_{\text{RF}}t)) &= 1 - \frac{(\Delta\varphi)^2}{4} - \frac{(\Delta\varphi)^2}{4} \cos(2\omega_{\text{RF}}t) \\ &\quad + \frac{(\Delta\varphi)^4}{64} + \frac{(\Delta\varphi)^4}{48} \cos(2\omega_{\text{RF}}t) \\ &\quad + \frac{(\Delta\varphi)^4}{192} \cos(4\omega_{\text{RF}}t) - \dots \end{aligned} \quad (9)$$

Thus, the denominator becomes:

$$\begin{aligned} D(t) &= \cos\theta(z) \left[1 - \frac{(\Delta\varphi)^2}{4} - \frac{(\Delta\varphi)^2}{4} \cos(2\omega_{\text{RF}}t) \right. \\ &\quad \left. + \frac{(\Delta\varphi)^4}{64} + \frac{(\Delta\varphi)^4}{48} \cos(2\omega_{\text{RF}}t) + \frac{(\Delta\varphi)^4}{192} \cos(4\omega_{\text{RF}}t) - \dots \right]. \end{aligned} \quad (10)$$

For small $\Delta\varphi$, we approximate the reciprocal $1/D(t)$ and define L_{J0} as:

$$L_{J0} = \frac{\Phi_0}{2\pi I_{c0} D_0} = \frac{\Phi_0}{2\pi I_{c0} \cos\theta(z) \left(1 - \frac{(\Delta\varphi)^2}{4} + \frac{(\Delta\varphi)^4}{64} \right)}, \quad (11)$$

where D_0 represents the average denominator. Then, the time-dependent modulation of the inductance is:

$$\delta L(z, t) = \frac{(\Delta\varphi)^2}{4D_0} \cos(2\omega_{\text{RF}}t). \quad (12)$$

The Josephson inductance becomes:

$$L_J(z, t) = L_{J0} (1 + \delta L(z, t)). \quad (13)$$

The wave equation for the voltage $V(z, t)$ along the transmission line derived from the telegrapher's for $L(z, t)$ varies slowly with time compared to the signal frequencies of interest and assuming a local relationship:

$$\frac{\partial^2 V(z, t)}{\partial z^2} - L(z, t) C \frac{\partial^2 V(z, t)}{\partial t^2} - C \frac{\partial L(z, t)}{\partial t} \frac{\partial V(z, t)}{\partial t} = 0. \quad (14)$$

where C is the capacitance per unit length of the transmission line. To address nonlocality, we reformulate the wave equation using a convolutional kernel or Green's function approach. These methods account for memory effects in the system, avoiding unphysical assumptions of instantaneous response. We proceed by updating the wave equation with a convolutional kernel and introducing a Volterra series expansion to capture the nonlinear and nonlocal effects. The kernel-based form of the wave equation that accounts for memory effects is given by:

$$\frac{\partial^2 V(z, t)}{\partial z^2} - C \frac{\partial}{\partial t} \left(\int_{-\infty}^t K(z, t - \tau) \frac{\partial V(z, \tau)}{\partial \tau} d\tau \right) = 0, \quad (15)$$

where $K(z, t - \tau)$ is the convolutional kernel representing the time-dependent, non-instantaneous response of the inductance. This integral form introduces a causal memory effect, where the voltage response at time t depends on the history of the voltage over $\tau < t$, ensuring that changes in inductance are correctly modeled over time. Expressing $V(z, t)$ as a nonlinear functional series, we

have:

$$V(z, t) = \sum_{n=1}^{\infty} \int_{-\infty}^t \cdots \int_{-\infty}^t H_n(z; t - \tau_1, \dots, t - \tau_n) \times \prod_{i=1}^n I(\tau_i) d\tau_1 \cdots d\tau_n, \quad (16)$$

where H_n are the Volterra kernels that capture the nonlinearity and nonlocal effects at different orders. Specifically, H_1 represents the first-order kernel (linear response), while H_2 and higher-order kernels capture the nonlinear responses. This expansion ensures that each order of nonlinearity is tied to a specific memory function, enabling complex interactions such as harmonic generation and nonlinear coupling to emerge naturally from the system dynamics. If we wish to handle spatial modulation explicitly, we can reformulate the equation using Green's functions. The Green's function $G(z, z'; t, \tau)$ represents the system's response at (z, t) due to a unit excitation at (z', τ) . For a spatially and temporally modulated inductance, the wave equation becomes:

$$V(z, t) = \int_{-\infty}^{\infty} \int_0^{\infty} G(z, z'; \tau) S(z', t - \tau) d\tau dz'. \quad (17)$$

where $G(z, z'; t - \tau)$ is the Green's function representing the system's impulse response in both space and time, and $S(z', \tau)$ is the source term, such as an external current or voltage source. This formulation inherently includes both time and spatial memory effects, allowing us to solve for $V(z, t)$ by convolution with the input source. With these tools, the full wave equation that includes nonlinearity and nonlocality is:

$$\begin{aligned} \frac{\partial^2 V(z, t)}{\partial z^2} - C \frac{\partial}{\partial t} \left(\int_{-\infty}^t K(z, t - \tau) \frac{\partial V(z, \tau)}{\partial \tau} d\tau \right) \\ - \sum_{n=2}^{\infty} \int \cdots \int H_n(z; t - \tau_1, \dots, t - \tau_n) \\ \times \prod_{i=1}^n I(\tau_i) d\tau_1 \cdots d\tau_n = 0. \end{aligned} \quad (18)$$

In this form, the convolutional term with $K(z, t - \tau)$ manages the non-instantaneous inductive response, the Volterra series terms H_n address higher-order nonlinear effects, and spatial nonlocality is inherently accounted for by the Green's function (if needed in an explicit form). The Energy modulation to second order in δL is expressed as:

$$P_{\text{mod}}(z, t) = \frac{1}{2} \frac{\partial L_J(z, t)}{\partial t} I^2(z, t) \quad (19)$$

To analyze the wave propagation, we employ coupled-mode theory by expressing $V(z, t)$ as a sum of harmonics:

$$V(z, t) = \sum_{n=-\infty}^{\infty} V_n(z) e^{-i(\omega + n\omega_{\text{RF}})t}, \quad (20)$$

where ω is the fundamental frequency, and $V_n(z)$ are the amplitudes of the harmonic components. Substituting and using $\delta L(z, t)$ from equation (12), we obtain:

$$\sum_n \left(\frac{d^2 V_n}{dz^2} + k_n^2 V_n \right) e^{-i(\omega + n\omega_{\text{RF}})t} + C \frac{\partial L_J(z, t)}{\partial t} \sum_n (\omega + n\omega_{\text{RF}}) V_n e^{-i(\omega + n\omega_{\text{RF}})t} = 0, \quad (21)$$

where $k_n^2 = L_{J0} C (\omega + n\omega_{\text{RF}})^2$. Collecting terms for each harmonic $e^{-i(\omega + n\omega_{\text{RF}})t}$, we obtain the coupled equations:

$$\frac{d^2 V_n}{dz^2} + k_n^2 V_n + \sum_m M_{n,m} V_m = 0, \quad (22)$$

where the coupling matrix $M_{n,m}$ is given by:

$$\begin{aligned} M_{n,n+2} &= -C (\omega + n\omega_{\text{RF}}) \\ &\left[(\omega + (n+2)\omega_{\text{RF}}) \delta L_{+2} + i \left(\frac{\partial L_J}{\partial t} \right)_{+2} \right], \\ M_{n,n-2} &= -C (\omega + n\omega_{\text{RF}}) \\ &\left[(\omega + (n-2)\omega_{\text{RF}}) \delta L_{-2} + i \left(\frac{\partial L_J}{\partial t} \right)_{-2} \right]. \end{aligned} \quad (23)$$

This modulation introduces coupling between modes with frequencies ω_n and $\omega_{n\pm 2}$, resulting in energy exchange between harmonics and the possibility of frequency conversion. The formation of bandgaps in the dispersion relation implies frequency ranges where wave propagation is prohibited, enabling the design of filters and isolators. Strong modulation requires retaining more terms in the expansion and necessitate numerical methods to solve the eigenvalue problem accurately. Applications include frequency conversion, nonreciprocal devices, parametric amplifiers, and qubit multiplexing in superconducting circuits.

Figure 2 provides a comprehensive analysis of the behavior of the space-time modulated JJ transmission line: (a) Dispersion Diagram: Shows the nonreciprocal nature of the medium, with clear asymmetry between forward and backward propagating harmonics, a key feature indicating breaking time-reversal symmetry. This nonreciprocity is crucial for phase matching and controlling harmonic interactions. (b) Time Evolution of Energy Transfer: Demonstrates how energy is redistributed from the fundamental mode to various harmonics over time, facilitated by space-time modulation. (c) Input Frequency Spectrum: Depicts the initial frequency content of the fundamental mode. (d) Generated Harmonics: Illustrates the effectiveness of frequency up-conversion in the modulated medium. (e) Radiation Pattern: Shows the resulting conversion of an initially isotropic source into 40 distinct beams, each precisely directed to a specific qubit in a ring connectivity array, exemplifying the capability of the medium to control beam steering and address individual qubits. These results confirm the ability of

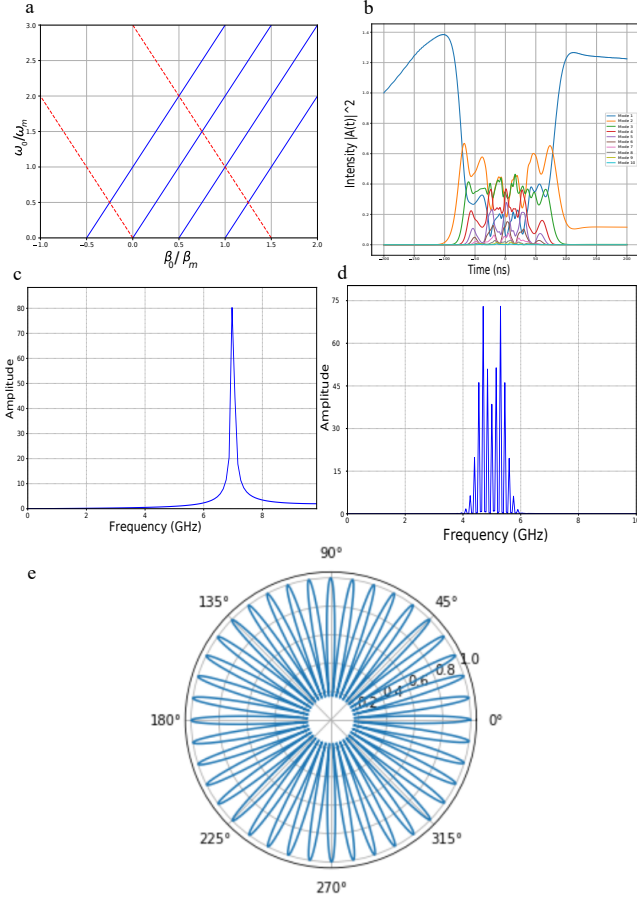


FIG. 2. (a) Dispersion diagram for modulation depth $\Delta I = 0.35$, showing asymmetry between forward and backward harmonics, indicative of nonreciprocity and phase matching of all forward harmonics as the system approaches the sonic regime. (b) Time evolution of energy transfer between 10 modes, illustrating how space-time modulation facilitates the distribution of energy from the fundamental mode to higher harmonics. (c) Input frequency spectrum of the fundamental mode. (d) Generated harmonics via frequency up-conversion in the modulated medium. (e) Radiation pattern showing conversion of an isotropic source into 40 directed beams, each addressing a specific qubit in a ring connectivity array, demonstrating precise beam steering and control of diffraction angles.

the metasurface to perform beam steering and frequency conversion, essential for multiplexed qubit control. The derived wave equation and beam control mechanisms provide a robust theoretical framework for understanding the dynamic behavior of the metasurface. To further explore and validate these effects, we employ numerical simulations using the Finite-Difference Time-Domain (FDTD) method. The goal of the numerical analysis is to visualize the wave propagation characteristics, investigate the impact of modulation on beam steering, and confirm key concepts such as frequency conversion and nonreciprocity. In the following section, we present the

numerical solution to the nonlinear wave equation. These simulations allow us to observe how the modulation parameters influence beam propagation in real time, providing insights into the practical applications of the metasurface in quantum computing. The nonlinearity and dispersion introduced by the modulation result in complex wave interactions, which will be explored in detail through the numerical results.

A. Qubit Interaction Using dynamic metasurface

Superconducting qubits are commonly controlled using microwave signals transmitted through coplanar waveguides or transmission lines. In our approach, we dynamically engineer the nonlinear wave propagation interactions to facilitate qubit control and entanglement by reconfigurably modulating the Josephson inductance. The time and spatial dependence of the inductance lead to a more complex wave equation, as expected when the permeability depends on both time and space. Moreover, convolution naturally arises due to the spatial modulation, which must be properly accounted for, even in the linear case. For small modulation depths, Δ_L , we neglect terms of order Δ_L^2 . We consider the modulation of the Josephson inductance as:

$$L_J(z, t) = L_{J0} [1 + \Delta_L \cos(k_m z - \omega_m t)], \quad (24)$$

where L_{J0} is the average Josephson inductance, $\Delta_L \ll 1$ is the modulation depth, and k_m and ω_m are the modulation wavenumber and frequency, respectively. The flux field $\Phi(z, t)$ satisfies the wave equation:

$$\frac{\partial}{\partial z} \left(\frac{1}{L_J(z, t)} \frac{\partial \Phi(z, t)}{\partial z} \right) - C_J \frac{\partial^2 \Phi(z, t)}{\partial t^2} = 0, \quad (25)$$

Assuming the modulation frequency ω_m matches the difference between adjacent mode frequencies, i.e., $\omega_m = \omega_{n+1} - \omega_n$, and considering only nearest-neighbor coupling, we can write:

$$\ddot{\Phi}_n(t) + \omega_n^2 \Phi_n(t) + \Delta_L \left(\frac{1}{2} \ddot{\Phi}_{n+1}(t) + \frac{k_m}{2L_{J0}C_J} \Phi_{n+1}(t) \right) e^{-i\omega_m t} + \Delta_L \left(\frac{1}{2} \ddot{\Phi}_{n-1}(t) - \frac{k_m}{2L_{J0}C_J} \Phi_{n-1}(t) \right) e^{i\omega_m t} = 0. \quad (26)$$

This set of equations represents the coupled-mode equations, where convolution in space is handled through the mode coupling induced by the modulation. Now, to quantize the system, we expand the flux field $\Phi(z, t)$ and promote its classical amplitudes to operators. The classical flux field is given by:

$$\Phi(z, t) = \sum_n \Phi_n(t) e^{ik_n z}. \quad (27)$$

Upon quantization, the field becomes:

$$\hat{\Phi}(z, t) = \sum_n \sqrt{\frac{\hbar}{2\omega_n C_J L}} (a_n e^{ik_n z} + a_n^\dagger e^{-ik_n z}), \quad (28)$$

where C_J is the capacitance per unit length, L is the inductance per unit length, and a_n, a_n^\dagger are the annihilation and creation operators. The interaction energy arises from the coupling of the qubit to this quantized flux. For a flux qubit, this coupling is proportional to the flux:

$$H_{int} = \alpha \hat{\sigma}_x \hat{\Phi}(z_q, t), \quad (29)$$

where α is a coupling constant and z_q is the qubit's position. Expanding this, we have:

$$H_{int} = \alpha \hat{\sigma}_x \sum_n \sqrt{\frac{\hbar}{2\omega_n C_J L}} (a_n e^{ik_n z_q} + a_n^\dagger e^{-ik_n z_q}). \quad (30)$$

The modulation of the inductance, $L_J(z, t) = L_{J0} [1 + \Delta_L \cos(k_m z - \omega_m t)]$, affects the coupling strength, leading to a time-dependent coupling:

$$\alpha(t) = \alpha_0 [1 + \Delta_L \cos(\omega_m t)], \quad (31)$$

where we have assumed the qubit is located at $z = 0$ for simplicity. Focusing on a single mode n , the interaction Hamiltonian simplifies to:

$$H_{int} = \hbar g(t) (\sigma_+ + \sigma_-) (a + a^\dagger), \quad (32)$$

where the time-dependent coupling strength is:

$$g(t) = g_0 [1 + \Delta_L \cos(\omega_m t)], \quad (33)$$

and $g_0 = \alpha_0 \sqrt{\frac{1}{2\hbar\omega_n C_J L_{J0}}}$.

B. The Sizzle Gate

The Sizzle gate is an entangling two-qubit gate that exploits the effective ZZ interaction arising in the dispersive regime of qubit coupling [?]. We consider two qubits located at positions z_1 and z_2 , coupled to a dynamic metasurface, such as a modulated nonlinear transmission line. The qubits interact with the metasurface through the Hamiltonian:

$$H_{int} = \hbar g_1 \sigma_x^{(1)} \Phi(z_1, t) + \hbar g_2 \sigma_x^{(2)} \Phi(z_2, t), \quad (34)$$

where g_j is the coupling strength of qubit j to the flux $\Phi(z, t)$, $\sigma_x^{(j)}$ is the Pauli-X operator for qubit j , and $\Phi(z, t)$ includes the effects of the modulation at frequency ω_m . The dynamic metasurface is modulated in both time and space at a frequency ω_m , with modulation depth ΔL , which adjusts the effective coupling between the qubits. The modulation introduces sidebands to the system, resulting in a rich spectrum of coupling pathways without the need to bring the qubits into resonance. Assuming that the qubits are detuned by $\Delta_{12} = \omega_{q1} - \omega_{q2}$, with $|\Delta_{12}| \gg g_j$, we operate in the dispersive regime. In this regime, direct exchange of excitations between the qubits

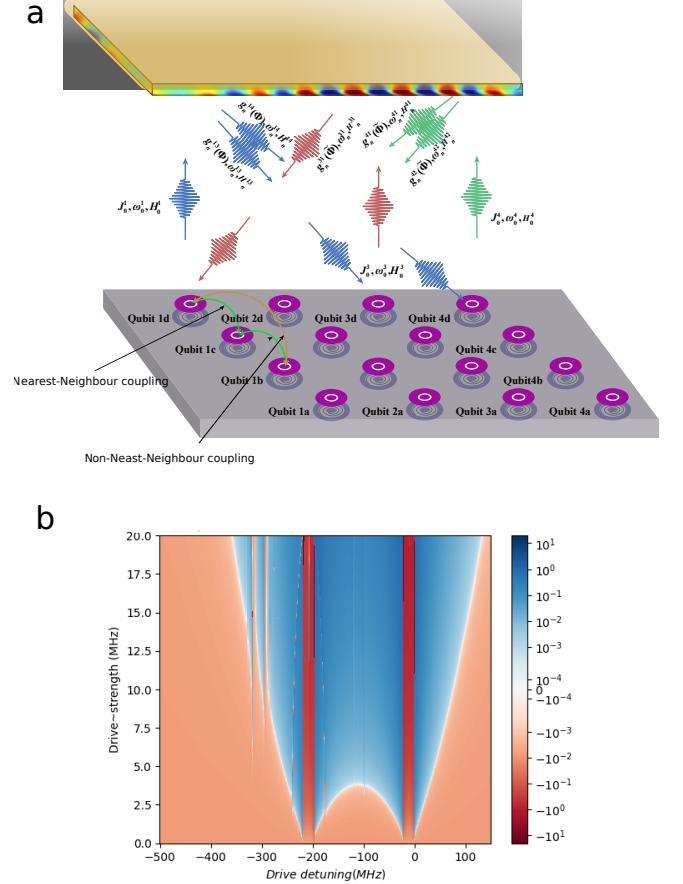


FIG. 3. (a) Illustration of a dynamic metasurface enabling two-qubit interactions through both nearest-neighbour and non-nearest-neighbour couplings. The metasurface modulates qubit photos beams frequencies (e.g. 3-8 GHz), generating harmonics that result in multi-beam diffraction at different angles. Central peaks correspond to the primary incident beams, while side peaks represent higher-order harmonics created by the modulated medium. This setup supports both next-nearest and non-nearest neighbour couplings. (b) Simulation of the effective ZZ interaction in a two-qubit Sizzle gate mediated by a dynamically modulated metasurface. The color map shows the ZZ interaction strength as a function of drive detuning and drive strength, where darker regions represent stronger interactions. Key parameters include qubit anharmonicities $\alpha_1 = 197$ MHz and $\alpha_2 = 195$ MHz, coupling strength $J = 0.7$ MHz, and detuning $\Delta = 133$ MHz. The modulation facilitates an off-resonant interaction that enables interaction without direct qubit-qubit resonance.

is suppressed, and virtual processes dominate the interaction. Updating the Hamiltonian to include the time-

space modulation, we get:

$$H_{\text{sizzle, mod}}/h = H_0/h + \sum_{i=0,1} \Omega_i(t, z_i) \cos(2\pi\nu_d t + \phi_i(t, z_i))(\hat{a}_i^\dagger + \hat{a}_i), \quad (35)$$

where $\Omega_i(t, z_i)$ and $\phi_i(t, z_i)$ now include modulation effects. Using second-order perturbation theory, we derive an effective Hamiltonian for the qubits that includes a ZZ interaction. The modulated metasurface mediates this interaction through virtual photon exchange. The interaction Hamiltonian can be written as:

$$H_{\text{eff}} = \hbar J_{\text{eff}} \left(\sigma_+^{(1)} \sigma_-^{(2)} + \sigma_-^{(1)} \sigma_+^{(2)} \right), \quad (36)$$

where J_{eff} is the effective exchange coupling between the qubits, modulated by the dynamic metasurface. The effective coupling J_{eff} arises due to virtual photon exchange mediated by the modulated modes of the dynamic metasurface. It is influenced by both the time and spatial modulation and is given by:

$$J_{\text{eff}} = \sum_{n,k} \frac{g_1 g_2 \delta_{n,k} \cos(k_m(z_1 - z_2))}{\Delta_{n,k}}, \quad (37)$$

where $\delta_{n,k}$ represents the modulation-induced coupling factors for the n -th mode and the k -th sideband, $\Delta_{n,k} = \omega_{q1} - (\omega_n \pm k\omega_m)$ is the effective detuning between qubit 1 and the k -th sideband of the n -th mode, and k_m is the wavevector of the modulation. The cosine term reflects the spatial dependence of the interaction due to the qubits' positions z_1 and z_2 . The sum is over the modes and sidebands that contribute to the interaction. If a dominant mode and sideband combination is found, the expression simplifies to:

$$J_{\text{eff}} \approx \frac{g_1 g_2 \delta \cos(k_m(z_1 - z_2))}{\Delta}, \quad (38)$$

where δ is the effective coupling factor for the dominant mode and sideband, and $\Delta = \omega_{q1} - (\omega_n \pm k\omega_m)$ is the corresponding detuning. Incorporating the time-space modulation into the ZZ interaction, the effective Hamiltonian becomes:

$$H_{\text{eff}}/h = \tilde{\nu}_{ZZ,\text{mod}} \sigma_z \otimes \sigma_z / 4 + \tilde{\nu}_{IZ,\text{mod}} \sigma_z \otimes I / 4 + \tilde{\nu}_{ZI,\text{mod}} I \otimes \sigma_z / 4, \quad (39)$$

where $\tilde{\nu}_{ZZ,\text{mod}}$, $\tilde{\nu}_{IZ,\text{mod}}$, and $\tilde{\nu}_{ZI,\text{mod}}$ now include modulation effects:

$$\tilde{\nu}_{ZZ,\text{mod}} = \tilde{\nu}_{ZZ} + \frac{2J\alpha_0\alpha_1\Omega_0\Omega_1 \cos(\phi_0 - \phi_1)}{(\Delta_{0,d} + \alpha_0)(\Delta_{1,d} + \alpha_1)\Delta_{0,d}\Delta_{1,d}}, \quad (40)$$

with Ω_i and ϕ_i as functions of time and space.

This Hamiltonian describes a ZZ interaction between the qubits, where the energy of each qubit depends on the state of the other qubit. The modulation parameters,

such as the modulation frequency ω_m , depth ΔL , and the wavevector k_m , control the effective coupling between the qubits. The gate time t_g for the Sizzle gate is determined by the accumulated phase due to the ZZ interaction. To achieve a desired controlled-Z (CZ) gate with phase θ , we set the interaction time such that:

$$\left(\frac{(J_{\text{eff}})^2}{\Delta_{12}} \right) t_g = \theta, \quad (41)$$

For a maximally entangling gate, such as a controlled-Z (CZ) gate where $\theta = \pi$, the interaction time is:

$$t_g = \frac{\pi \Delta_{12}}{(J_{\text{eff}})^2}. \quad (42)$$

The Sizzle gate thus effectively uses the ZZ interaction derived from the exchange coupling in the dispersive regime to implement a controlled-phase gate. By keeping the qubits detuned and modulating the dynamic metasurface, we can implement high-fidelity entangling gates without the need to bring the qubits into resonance.

III. NUMERICAL SOLUTION OF THE NONLINEAR WAVE EQUATION WITH TIME-SPACE MODULATION

We solve the nonlinear wave equation (Eq. (18)) using the Finite-Difference Time-Domain (FDTD) method. This method discretizes both space and time, representing $\phi(z, t)$ as ϕ_i^n , where i and n are spatial and temporal grid indices, respectively:

$$\phi(z, t) \rightarrow \phi_i^n, \quad z = i\Delta z, \quad t = n\Delta t.$$

We approximate the derivatives using central differences. For time derivatives:

$$\frac{\partial \phi}{\partial t} \Big|_i^n \approx \frac{\phi_i^{n+1} - \phi_i^{n-1}}{2\Delta t}, \quad \frac{\partial^2 \phi}{\partial t^2} \Big|_i^n \approx \frac{\phi_i^{n+1} - 2\phi_i^n + \phi_i^{n-1}}{(\Delta t)^2}, \quad (43)$$

For spatial derivatives:

$$\frac{\partial \phi}{\partial z} \Big|_i^n \approx \frac{\phi_{i+1}^n - \phi_{i-1}^n}{2\Delta z}, \quad \frac{\partial^2 \phi}{\partial z^2} \Big|_i^n \approx \frac{\phi_{i+1}^n - 2\phi_i^n + \phi_{i-1}^n}{(\Delta z)^2}. \quad (44)$$

Higher-order mixed derivatives are given by:

$$\frac{\partial^4 \phi}{\partial z^2 \partial t^2} \Big|_i^n \approx \frac{1}{(\Delta z)^2 (\Delta t)^2} (\phi_{i+1}^{n+1} - 2\phi_i^{n+1} + \phi_{i-1}^{n+1} - 2(\phi_{i+1}^n - 2\phi_i^n + \phi_{i-1}^n) + \phi_{i+1}^{n-1} - 2\phi_i^{n-1} + \phi_{i-1}^{n-1}). \quad (45)$$

Substituting the central difference approximations into the wave equation, we obtain the fully discrete equation:

$$\begin{aligned}
& C \left(\frac{\phi_i^{n+1} - 2\phi_i^n + \phi_i^{n-1}}{(\Delta t)^2} \right) \\
& - C_J a^2 \left(\frac{\phi_{i+1}^{n+1} - 2\phi_i^{n+1} + \phi_{i-1}^{n+1}}{(\Delta z)^2 (\Delta t)^2} - 2(\phi_{i+1}^n - 2\phi_i^n + \phi_{i-1}^n) \right. \\
& \quad \left. + \phi_{i+1}^{n-1} - 2\phi_i^{n-1} + \phi_{i-1}^{n-1} \right) \\
& + \frac{I_{c0} \Delta_I k_m}{\varphi_0} a \sin(k_m z_i - \omega_m t_n) \sin \phi_i^n \\
& - \frac{I_c(z_i, t_n)}{\varphi_0} \left(a \cos \phi_i^n \frac{\phi_{i+1}^n - \phi_{i-1}^n}{2\Delta z} \right. \\
& \quad \left. - a^2 \sin \phi_i^n \left(\frac{\phi_{i+1}^n - \phi_{i-1}^n}{2\Delta z} \right)^2 \right) = 0. \quad (46)
\end{aligned}$$

This equation allows us to solve for ϕ_i^{n+1} in terms of previously known values at time step n . By discretizing both time and space, we represent the field $\phi(z, t)$ at discrete points on a grid, allowing us to compute wave propagation in a modulated transmission line. The central difference approximations for time and space derivatives are applied to convert the continuous wave equation into a fully discrete form, which is iteratively solved to model wave evolution over time. We begin by setting the initial conditions for ϕ_i^0 and ϕ_i^1 , which represent the field at the first two time steps. Depending on the physical scenario, this could be a Gaussian pulse or sinusoidal wave. Additionally, the initial time derivative $\left. \frac{\partial \phi}{\partial t} \right|_{t=0}$ is needed to compute ϕ_i^1 . Appropriate boundary conditions are applied at the edges of the computational domain. For open boundaries, we use Mur's first-order absorbing boundary conditions to minimize reflections, allowing waves to propagate out of the domain without artificial reflections. Alternatively, periodic or fixed boundary conditions may be applied depending on the specific problem. The time-stepping process involves updating the field ϕ_i^{n+1} at each grid point i for each time step n , using the fully discretized equation. The nonlinear terms, such as $\sin \phi_i^n$, $\cos \phi_i^n$, and spatial derivatives $\left(\frac{\phi_{i+1}^n - \phi_{i-1}^n}{2\Delta z} \right)^2$, are computed at the current time step. To ensure numerical stability, we select Δt and Δz based on the Courant-Friedrichs-Lewy (CFL) condition $\Delta t \leq \Delta z/v_{\max}$ and $S = \frac{c\Delta t}{\sqrt{(\Delta x)^2 + (\Delta z)^2}} \leq \frac{1}{\sqrt{2}}$. However, due to nonlinearity and dispersion, a more stringent condition may be required, which can be determined through von Neumann stability analysis. Relevant quantities, such as ϕ_i^n , $\frac{\partial \phi_i^n}{\partial t}$, and other derived fields, are recorded for the analysis of phenomena like frequency conversion, parametric amplification, and dispersion characteristics.

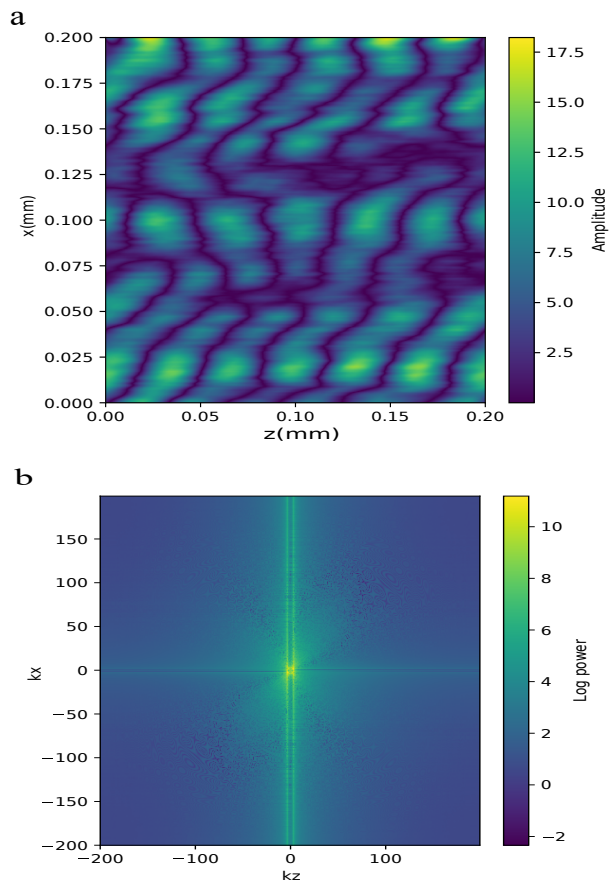


FIG. 4. (a) Spatial amplitude distribution in the time-space modulated Josephson Junction transmission line showing wave interference in the $x - z$ plane. (b) Illustration of the conversion of the incident wave to surface waves along k_z and k_x , with multiple beams formed at different angles.

A. Simulation Results

We present the FDTD simulation results for wave propagation in a space-time modulated superconducting metasurface. The incident wave is modulated with a Gaussian envelop and an incident wave frequency of 5 GHz. The spatial grid resolution is set at $\lambda_0/25$ with time step determined by the Courant condition. Mur boundary conditions are applied to minimize reflections. Figure 4 illustrates the spatial and spectral characteristics of the wave propagation in a time-space modulated Josephson Junction transmission line. In (a), the spatial distribution of the wave amplitude is shown in the $x - z$ plane. The interference pattern is a result of the modulation, with distinct regions of high (yellow) and low (purple) amplitudes. Figure 4 (b) presents an illustration of the spatial pattern, revealing the incident wave propagation out of the plane. Notably, the wave is converted into surface waves along the k_z and k_x

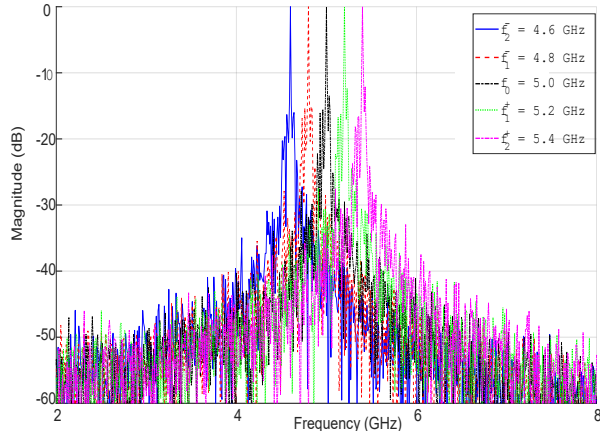


FIG. 5. Frequency spectra of incident and diffracted beams for various input frequencies (4.6-5.4 GHz). Central peaks represent incident beams, while side peaks show harmonics generated by the modulated medium, illustrating multi-beam formation at different angles. The amplitude is normalized for clarity of comparison across different frequency ranges.

directions, with the formation of multiple beams at different angles. These beams correspond to energy redistribution into various harmonic modes, as shown by the bright spots in the logarithmic power spectrum.

Figure 5 Frequency spectrum analysis of multi-beam formation in a modulated medium. The Fourier transform illustrates the frequency content of the incident beam (central peak) and the generation of multiple harmonics (side peaks) corresponding to diffracted beams at various angles. Each color represents a different fundamental frequency (f_0) of the incident wave, ranging from 4.6 GHz to 5.4 GHz. The plot demonstrates how the modulation of the medium leads to frequency mixing, resulting in the creation of new frequency components and the spatial separation of beams.

IV. DISCUSSION AND OUTLOOK

This work underscores the potential of space-time modulated Josephson Junction (JJ) metasurfaces in achieving scalable, hardware-efficient control of superconducting qubits. By harnessing the nonlinear dynamics and modulation capabilities inherent in JJ arrays, the

proposed architecture addresses significant challenges associated with scaling quantum processors. Notably, it mitigates wiring complexity and reduces thermal loads—critical factors when scaling to large qubit numbers. The ability to multiplex control signals through beam steering and frequency conversion allows for the simultaneous operation of multiple qubits using a single input, significantly simplifying the control infrastructure. The metasurface architecture also enables the multiplexing of control signals to multiple qubits by modulating different regions to generate pulses with varying frequencies or phases, minimizing hardware overhead.

Challenges remain in achieving the necessary modulation depth and frequency precision to avoid errors that affect gate fidelity. Material choices for JJs impact performance, with materials such as NbN/AlN/NbN [28] offering stronger modulation and higher signal amplitudes but introducing fabrication complexities and potential microwave losses. Thermal management is another critical factor. While the metasurface reduces the number of control lines, the modulation process itself can introduce thermal loads that must be managed within the cooling capacity of dilution refrigerators. Crosstalk and interference between control signals must be mitigated using strategies such as spatial filtering, frequency multiplexing, and advanced modulation schemes.

Future work will focus on experimental prototyping of the metasurface, optimizing modulation schemes, addressing thermal management, and exploring modulation techniques like adaptive modulation driven by real-time feedback. Implementing error mitigation strategies and studying scalability will be critical for evaluating the metasurface’s performance as qubit counts increase. The successful execution of quantum algorithms using metasurface-controlled qubits will be a key milestone, demonstrating the practical benefits of this approach. In conclusion, space-time modulated JJ metasurfaces offer a promising path towards scalable and hardware-efficient qubit control. Interdisciplinary collaboration across superconducting electronics, quantum information science, and materials engineering will be crucial to realizing the full potential of this approach and accelerating the development of large-scale quantum processors.

ACKNOWLEDGMENTS

M. Bakr acknowledges support from EPSRC QT Fellowship Grant EP/W027992/1. We thank Smain Amari and Mohammed Alghadeer for insightful discussions.

[1] P. A. Spring, S. Cao, T. Tsunoda, G. Campanaro, S. Fasciati, J. Wills, M. Bakr, V. Chidambaram, B. Shteynas, L. Carpenter, *et al.*, “High coherence and low cross-talk in a tileable 3D integrated superconducting circuit architecture,” *Science Advances*, **8**(16), eab16698, 2022.

[2] D. D. Awschalom, L. C. Bassett, A. S. Dzurak, E. L. Hu, and J. R. Petta, “Quantum Spintronics: Engineering and Manipulating Atom-Like Spins in Semiconductors,” *Science*, **339**(6124), 1174–1179, 2013. doi: [10.1126/science.1231364](https://doi.org/10.1126/science.1231364).

- [3] M. Bakr *et al.*, “Hybrid 2D/3D integrated readout multiplexing in circuit QED,” *Bulletin of the American Physical Society*, 2022.
- [4] S. Taravati and M. Bakr, “Nonlinear space-time modulation for exquisite wavecrafting in superconducting quantum systems,” *Bulletin of the American Physical Society*, 2024.
- [5] S. Cao, M. S. Bakr, G. Campanaro, S. Fasciati, J. Wills, D. K. Lall, B. Shteynas, V. Chidambaram, I. Rungger, and P. J. Leek, “Emulating two qubits with a four-level transmon qudit for variational quantum algorithms,” *Quantum Science and Technology*, **9**, 2023. Available: <https://api.semanticscholar.org/CorpusID:257404976>.
- [6] S. Krinner, S. Storz, P. Kurpiers, P. Magnard, J. Heinsoo, R. Keller, J. Luetolf, C. Eichler, and A. Wallraff, “Engineering cryogenic setups for 100-qubit scale superconducting circuit systems,” *EPJ Quantum Technology*, **6**, 1–29, 2018. Available: <https://api.semanticscholar.org/CorpusID:51682821>.
- [7] F. Lecocq, F. Quinlan, K. Cicak, J. Aumentado, S. A. Diddams, and J. D. Teufel, “Control and readout of a superconducting qubit using a photonic link,” *Nature*, **591**, 575–579, 2020. Available: <https://api.semanticscholar.org/CorpusID:221446137>.
- [8] R. Acharya *et al.*, “Multiplexed superconducting qubit control at millikelvin temperatures with a low-power cryo-CMOS multiplexer,” *Nature Electronics*, **6**(11), 900–909, 2023. doi: [10.1038/s41928-023-01033-8](https://doi.org/10.1038/s41928-023-01033-8).
- [9] A. G. Fowler, M. Mariantoni, J. M. Martinis, and A. N. Cleland, “Surface codes: Towards practical large-scale quantum computation,” *Physical Review A*, **86**, 032324, 2012. Available: <https://api.semanticscholar.org/CorpusID:119277773>.
- [10] M. Kjaergaard, M. E. Schwartz, J. Braumuller, P. Krantz, J. I-Jan Wang, S. Gustavsson, and W. D. Oliver, “Superconducting Qubits: Current State of Play,” *Annual Review of Condensed Matter Physics*, 2019. Available: <https://api.semanticscholar.org/CorpusID:173188891>.
- [11] K. Li, R. McDermott, and M. G. Vavilov, “Hardware-Efficient Qubit Control with Single-Flux-Quantum Pulse Sequences,” *Physical Review Applied*, **12**(1), 014044, 2019. doi: [10.1103/PhysRevApplied.12.014044](https://doi.org/10.1103/PhysRevApplied.12.014044).
- [12] A. J. Sirois, M. A. Castellanos-Beltran, A. E. Fox, S. P. Benz, and P. F. Hopkins, “Josephson Microwave Sources Applied to Quantum Information Systems,” *IEEE Transactions on Quantum Engineering*, **1**, 1–7, 2020. Available: <https://api.semanticscholar.org/CorpusID:231644887>.
- [13] L. Casparis, N. Pearson, A. Kringhøj, T. W. Larsen, F. Kuemmeth, J. Nygård, P. Krogstrup, K. D. Petersson, and C. M. Marcus, “Voltage-controlled superconducting quantum bus,” *Physical Review B*, 2018. Available: <https://api.semanticscholar.org/CorpusID:54995774>.
- [14] J. Braumuller, L. Ding, A. Vepsalainen, Y. Sung, M. Kjaergaard, T. Menke, R. Winik, D. K. Kim, B. M. Niedzielski, A. Melville, J. L. Yoder, C. F. Hirjibehedin, T. P. Orlando, S. Gustavsson, and W. D. Oliver, “Characterizing and Optimizing Qubit Coherence Based on SQUID Geometry,” *arXiv: Quantum Physics*, 2020. Available: <https://api.semanticscholar.org/CorpusID:211252432>.
- [15] A. Bargerbos, L. J. Splitthoff, M. Pita-Vidal, J. J. Wessdorp, Y. Liu, P. Krogstrup, L. P. Kouwenhoven, C. K. Andersen, and L. Grünhaupt, “Mitigation of Quasiparticle Loss in Superconducting Qubits by Phonon Scattering,” *Physical Review Applied*, **19**(2), 024014, 2023. doi: [10.1103/PhysRevApplied.19.024014](https://doi.org/10.1103/PhysRevApplied.19.024014).
- [16] M. J. Reagor, C. Osborn, N. A. Tezak, A. Staley, G. E. D. K. Prawiroatmodjo, M. G. Scheer, N. Alidoust, E. A. Sete, N. Didier, M. P. da Silva, *et al.*, “Demonstration of universal parametric entangling gates on a multi-qubit lattice,” *Science Advances*, **4**, 2017. Available: <https://api.semanticscholar.org/CorpusID:13687098>.
- [17] J. Koch, T. M. Yu, J. M. Gambetta, A. A. Houck, D. I. Schuster, J. Majer, A. Blais, M. H. Devoret, S. M. Girvin, and R. J. Schoelkopf, “Charge-insensitive qubit design derived from the Cooper pair box,” *Physical Review A*, **76**, 042319, 2007. Available: <https://api.semanticscholar.org/CorpusID:53983107>.
- [18] Y. Ueno, S. Imamura, Y. Tomida, T. Tanimoto, M. Tanaka, Y. Tabuchi, K. Inoue, and H. Nakamura, “SFQ counter-based precomputation for large-scale cryogenic VQE machines,” *arXiv:2403.00363*, 2025.
- [19] M. R. Jocar, R. Rines, and F. T. Chong, “Practical implications of SFQ-based two-qubit gates,” in *2021 IEEE International Conference on Quantum Computing and Engineering (QCE)*, 402–412, 2021. doi: [10.1109/QCE52317.2021.00061](https://doi.org/10.1109/QCE52317.2021.00061).
- [20] V. Vozhakov, M. Bastrakova, N. Klenov, A. Satanin, and I. Soloviev, “Speeding up qubit control with bipolar single-flux-quantum pulse sequences,” *Quantum Science and Technology*, **8**, 2023.
- [21] Y. Xu, G.-M. Huang, J. Balewski, A. Morvan, K. Nowrouzi, D. I. Santiago, R. K. Naik, B. K. Mitchell, and I. Siddiqi, “Automatic Qubit Characterization and Gate Optimization with QubiC,” *ACM Transactions on Quantum Computing*, **4**, 1–12, 2021. Available: <https://api.semanticscholar.org/CorpusID:233346887>.
- [22] Y. Xu, G. Huang, J. Balewski, R. Naik, A. Morvan, B. Mitchell, K. Nowrouzi, D. I. Santiago, and I. Siddiqi, “QubiC: An Open-Source FPGA-Based Control and Measurement System for Superconducting Quantum Information Processors,” *IEEE Transactions on Quantum Engineering*, **2**, 2021. doi: [10.1109/TQE.2021.3116540](https://doi.org/10.1109/TQE.2021.3116540).
- [23] E. Charbon, F. Sebastiano, A. Vladimirescu, H. Homulle, S. Visser, L. Song, and R. M. Incandela, “Cryo-CMOS for quantum computing,” in *2016 IEEE International Electron Devices Meeting (IEDM)*, 13.5.1–13.5.4, 2016. doi: [10.1109/IEDM.2016.7838410](https://doi.org/10.1109/IEDM.2016.7838410).
- [24] A. Potočnik, S. Brebels, J. Verjauw, R. Acharya, A. Grill, D. Wan, M. Mongillo, R. Li, T. Ivanov, S. Van Winckel, F. A. Mohiyaddin, B. Govoreanu, J. Craninckx, and I. P. Radu, “Millikelvin temperature cryo-CMOS multiplexer for scalable quantum device characterisation,” *Quantum Science & Technology*, **7**, 2020. Available: <https://api.semanticscholar.org/CorpusID:227127133>.
- [25] P. Shi, J. Yuan, F. Yan, and H. Yu, “Multiplexed control scheme for scalable quantum information processing with superconducting qubits,” *arXiv:2312.06911*, 2023.
- [26] S. Meesala, S. Wood, D. Lake, P. Chiappina, C. Zhong, A. D. Beyer, M. D. Shaw, L. Jiang, and O. Painter, “Non-classical microwave-optical photon pair generation with a chip-scale transducer,” *Nature Physics*, **20**(5), 871–877, 2024. doi: [10.1038/s41567-024-02409-z](https://doi.org/10.1038/s41567-024-02409-z).
- [27] J. M. Hornibrook *et al.*, “Cryogenic Control Architecture

- for Large-Scale Quantum Computing,” *Physical Review Applied*, **3**(2), 024010, 2015. doi: [10.1103/PhysRevApplied.3.024010](https://doi.org/10.1103/PhysRevApplied.3.024010).
- [28] S. Kim, H. Terai, T. Yamashita, W. Qiu, T. Fuse, F. Yoshihara, S. Ashhab, K. Inomata, and K. Semba, “Enhanced coherence of all-nitride superconducting qubits epitaxially grown on silicon substrate,” *Communications Materials*, **2**, 2021. Available: <https://api.semanticscholar.org/CorpusID:237566595>.